Author/s:
Kermaniyan, SS;Chen, M;Zhang, C;Smith, SA;Johnston, APR;Such, C;Such, GK

Title:
Understanding the Biological Interactions of pH-Swellable Nanoparticles

Date:
2022-05-01

Citation:
Kermaniyan, S. S., Chen, M., Zhang, C., Smith, S. A., Johnston, A. P. R., Such, C. & Such, G. K. (2022). Understanding the Biological Interactions of pH-Swellable Nanoparticles. Macromolecular Bioscience, 22 (5), https://doi.org/10.1002/mabi.202100445.

Persistent Link:
https://hdl.handle.net/11343/320349

Macromolecular Bioscience
www.mbs-journal.de

Understanding the Biological Interactions of pH-Swellable Nanoparticles

*Sarah S. Kermaniyan, Moore Chen, Changhe Zhang, Samuel A. Smith, Angus P. R. Johnston, Chris Such, and Georgina K. Such**

pH-responsive nanoparticles have generated significant interest for use as drug delivery systems due to their potential for inducible release at low pH. The pH variation from the bloodstream (pH 7.4) to intracellular compartments of cells called endosomes/lysosomes (pH < 5.0) has been of particular interest. However, one of the limitations with nanoparticle delivery systems is the inability to migrate out of these compartments to the cytosol or other organelles, via a process termed endosomal escape. Previous studies have postulated that pH-responsive nanoparticles can facilitate endosomal escape through a range of mechanisms including membrane interaction, pH-induced swelling, and the proton-sponge effect. In this study, a series of pH-swellable nanoparticles (85–100 nm) are designed and their impact on biological interactions, particularly endosomal escape, are investigated. The particles exhibit tunable pH-induced swelling (from 120% to 200%) and have good buffering capacity. The cellular association is studied using flow cytometry and endosomal escape is determined using a calcein leakage assay. Interestingly, no endosomal escape with all nanoparticle formulations is found, which suggests there are limitations with both the proton-sponge effect and pH-induced swelling mechanism as the primary methods for inducing endosomal escape.

1. Introduction

Many studies have demonstrated the potential of polymeric nanocarriers to provide more efficient delivery of therapeutics to target sites.[15] They have many advantages including the protection of hydrophilic/hydrophobic cargo in the body until it gets to a site of action, and the controllable delivery of cargo to specific diseased cells.[5,6] However, there remain many challenges to achieve successful drug delivery.[5,6] One of the critical bottlenecks is endosomal escape.[7] Nanoparticles are taken up into cells through various endocytic pathways.[8] They are then entrapped in acidic compartments called endosomes (≈ pH 5.5),[9] which subsequently mature into late endosome/lysosomes (< pH 5.0).[9] Particles need to escape these acidic endo/lysosomal compartments as it is not the site of action for most cargos. Localization in the endosome/lysosome is particularly problematic for biological cargos such as DNA or proteins due to premature degradation.[5,9]

A number of different materials have been used to engineer endosomal escape including pH-responsive polymers, cell-penetrating peptides, and liquid metal transformers.[7,10] One important family of materials is charge-shifting polymers such as poly(2-diisopropylamino ethyl methacrylate) (PDPA) with the pK_a value of ≈ 6.4 and poly(2-diethylamino ethyl methacrylate) (PDEA) with the pK_a value of ≈ 7.0.[10,11,7] The amine groups in these polymers are protonated when pH decreases to below the pK_a, and this induces a hydrophobic to hydrophilic switch in the polymer. A transition in this pH range is of interest for delivery systems as it corresponds to the drop in pH that occurs upon particle internalization inside the body.[10,6,7]

Many reports have hypothesized that charge-shifting nanoparticles can facilitate endosomal escape through the disassembly of particles, with membrane interactions impacted by properties such as hydrophobicity, morphology, and pH transition of the polymers used to assemble the particles (**Scheme 1**A).[12,13] Other studies have concluded that endosomal escape can occur through mechanical strain of the endosomal membrane due to the swelling of particles induced by a decrease in pH (Scheme 1B).[11,14] There is also significant work postulating that the proton-sponge effect is a critical factor for inducing escape (Scheme 1C). The proton-sponge mechanism states that protonation triggers an influx of protons to inhibit the drop in pH, and chloride ions to avoid the charge gradient resulted from

S. S. Kermaniyan, C. Zhang, S. A. Smith, C. Such, G. K. Such
School of Chemistry
The University of Melbourne
Parkville, Victoria 3010, Australia
E-mail: gsuch@unimelb.edu.au

M. Chen, A. P. R. Johnston
Monash Institute of Pharmaceutical Sciences
Monash University
Parkville, Victoria 3052, Australia

The ORCID identification number(s) for the author(s) of this article can be found under https://doi.org/10.1002/mabi.202100445

DOI: 10.1002/mabi.202100445

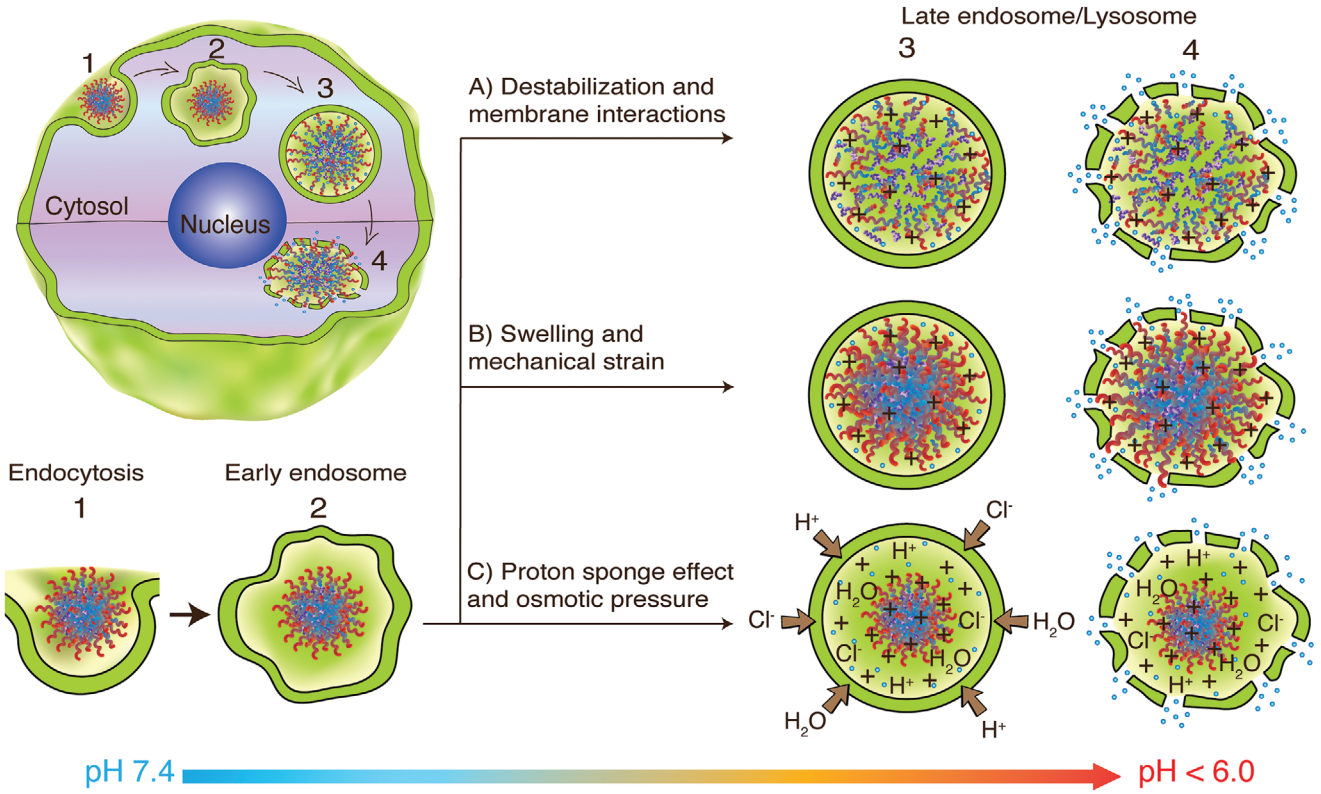

Scheme 1. Schematic of commonly proposed endosomal escape mechanisms, A) membrane destabilization, B) nanoparticle swelling, and C) proton-sponge effect.

the influx of protons.[15,7] Pumping both protons and chloride ions increases the osmolarity of the endosome causing water absorption.[15,6,7] This large inflow of ions leads to an osmotic swelling (in cross-linked/non-cross-linked particles) and eventually membrane lysis.[1618] The pH-induced swelling mechanism most commonly occurs alongside the proton-sponge effect as materials act as a buffer as they become protonated. Previous work has postulated that swelling causes both mechanical pressure on the membrane and buffering to induce destruction of the endosomal membrane. Irvine and co-workers reported a swellable pH-responsive nanoparticle with a pH-sensitive PDEA core and a pH-insensitive poly(aminoethyl methacrylate) shell cross-linked with poly(ethylene glycol) dimethacrylate.[11] A 2.8-fold increase in the size of particles (from 200 to 550 nm) was observed when pH was decreased from 7.4 to 4.9.[11] The effective release of calcein and the protein ovalbumin into the cytosol of DC2.4 cell line was shown, which was attributed to a combination of an increase in osmotic pressure due to the proton-sponge effect and the mechanical strain of the pH-induced particle swelling.[11] In a related study, a polyion complex was synthesized based on PEGylated polyamine nanogels composed of a chemically crosslinked PDEA core surrounded by PEG tethered chains to deliver siRNA.[19] These nanogels swelled from 81 nm at pH 7.4 to 134 nm at pH 5.5. The observed endosomal escape was ascribed to the buffering capacity of DEA core and the proton-sponge effect.[19]

Herein, we designed a set of new pH-swellable particles with tunable onset of swelling (the swelling percentage and the swelling pH) and investigated the impact of nanoparticle structure on biological interactions. Emulsion nanoparticles with different ratios of 2-diisopropylamino ethyl methacrylate (DPA) and 2-diethylamino ethyl methacrylate (DEA) were prepared, referred to as DPA_1DEA_2, DPA_2DEA_1, and DPA_3DEA_0. These pH-responsive nanoparticles were highly uniform and stable between pH 7.4 and 5.0 and showed strong pH buffering capacity. The particles also demonstrated significant swelling from ≈ 85–100 nm at pH 7.4 to ≈ 200–300 nm at low pH, with swelling induced between pH 6.0 and 5.6. The particles showed different cellular association based on the composition of the charge-shifting monomers. Interestingly, despite swelling to between 120% and 200% of their original size, their strong buffering capacity, and high levels of cellular association, none of the particles induced endosomal escape of calcein. Endosomal escape properties of these particles would be predicted by both the pH-induced swelling mechanism and the proton-sponge effect. This shows the need for further investigation on the underlying mechanisms driving endosomal escape of nanoparticles, in order to engineer better nanoparticles in the future.

2. Experimental Section

2.1. Materials

Poly(ethylene glycol) methyl ether methacrylate (PEGMA, the number average molecular weight (M_n) 300, contains 100 ppm MEHQ as inhibitor, 300 ppm BHT as inhibitor),

poly(ethylene oxide) monomethyl ether (mPEG-OH, average M_n ≈2000, flakes), butyl acrylate (BA, ≥ 99%, contains 10–60 ppm monomethyl ether hydroquinone as inhibitor, molecular weight 128.17 g mol^{-1}), 4-cyano-4-(phenylcarbonothioylthio) pentanoic acid (molecular weight 279.38 g mol^{-1}), *N*-hydroxysuccinimide (molecular weight 115.09 g mol^{-1}),*N,N'*-diisopropylcarbodiimide (DIC, molecular weight 126.20 g mol^{-1}), *N,N'*-dicyclohexylcarbodiimide (DCC, molecular weight 206.33 g mol^{-1}), 4-(dimethylamino)pyridine (DMAP, molecular weight 122.17 g mol^{-1}), *α,α'*-azobisisobutyronitrile (AIBN, molecular weight 164.21 g mol^{-1}), 1,4-dioxane (molecular weight 88.11 g mol^{-1}), dichloromethane (DCM, molecular weight 84.93 g mol^{-1}), 2-(diisopropylamino)ethyl methacrylate (DPA, molecular weight 213.32 g mol^{-1}), 2-(diethylamino)ethyl methacrylate (DEA, molecular weight 185.26 g mol^{-1}), 4,4'-Azobis(4-cyano valeric acid) (ABCVA, molecular weight 280.28 g mol^{-1}), *N,N*-dimethylformamide (DMF, molecular weight 73.09 g mol^{-1}), triethylamine (TEA, molecular weight 101.19 g mol^{-1}), methacrylic acid (molecular weight 86.09 g mol^{-1}), sodium chloride (NaCl, molecular weight 58.44 g mol^{-1}), potassium chloride (KCl, molecular weight 74.55 g mol^{-1}), sodium phosphate dibasic (Na_2HPO_4, molecular weight 141.96 g mol^{-1}), potassium phosphate monobasic (KH_2PO_4, molecular weight 136.09 g mol^{-1}), and maleic acid (molecular weight 116.07 g mol^{-1}) were purchased from Sigma–Aldrich. Cyanine 5 amine (Cy5, molecular weight 653.77 g mol^{-1}) was bought from the Lumiprobe company. The water used in all experiments was obtained from the distilled water (DI) tap.

2.2. Characterization

Nuclear magnetic resonance (^{1}H NMR) spectra were obtained on Agilent MR400 MHz and Agilent DD2 500 MHz NMR spectrometers at room temperature. Chemical shifts (δ_H) were reported in parts per million (ppm). Deuterated chloroform ($CDCl_3$: δ_H 7.25 ppm) and deuterium oxide (D_2O: δ_H 4.80 ppm) were used for ^{1}H NMR characterization. ^{1}H NMR analysis was performed on MestreNova software.

Gel permeation chromatography (GPC) analysis was conducted with a Shimadzu system equipped with a CMB-20A controller system and a Waters Styragel column (10 μm pore size). DMAc containing 4.3 g L^{-1} lithium bromide and chromatography grade tetrahydrofuran (THF) were used as the eluents with a flow rate of 0.3 mL min^{-1} at 50 °C. The molecular weight and polydispersity of the samples were calculated relative to poly(methyl methacrylate) standards.

MALDI-TOF (autoflex III smartbeam) was used to obtain the molecular weight of the stabilizer. The matrix (*trans*-2-(3-*tert*-Butyl-Phenyl)-2-methyl-2-propenylidene)malononitrile), sample, and salt (potassium trifluoroacetate) were dissolved in DCM, methanol, and methanol separately at the concentrations of ≈ 1 mg mL^{-1}. Then these three solutions were mixed in a volume ratio of 10:1:1. Approximately 0.3 μL of the mixture was then spotted on the target plate for measurements.

The size and polydispersity of particles were recorded on dynamic light scattering (DLS) (Horiba Scientific, SZ-100) at a fixed scattering angle of 90°. DLS was conducted with three measurements at 37 °C. Particles were diluted in phosphate-buffered saline (PBS with 10×10^{-3} M Na_2HPO_4, 137×10^{-3}M NaCl, 2.7×10^{-3} M KCl, and 1.8×10^{-3} M KH_2PO_4), at the volume ratio 20:480 and at different pH values ranging from pH 7.4 to pH 5.0 (pH adjustments were done by a Mettler Toledo pH meter). The nanoparticles were incubated at 37 °C for ≈ 2 min at different pH levels before each measurement. To obtain PBS with 10×10^{-3} M Na_2HPO_4, 2 L of 0.2 M PBS stock solution was prepared using NaCl (320 g, 5.48 mol), KCl (8 g, 107.31 mmol), KH_2PO_4 (9.6 g, 70.54 mmol), and Na_2HPO_4 (57.60 g, 405.75 mmol). The 0.2 M PBS stock solution was then diluted to be 10×10^{-3} M before use.

Zeta potential was measured by using a Brookhaven instrument (PALS zeta potential analyzer). Particles were dialyzed against water, then after freeze-drying, 0.6 mg solid particles were mixed with 1.5 mL of phosphate buffer (1.42 g L^{-1} Na_2HPO_4 and 0.24 g L^{-1} KH_2PO_4) at pH 7.4 and at the corresponding low pH values of 5.8, 5.6, and 5.4. Then, the zeta potential of each particle was measured at pH 7.4 and low pH corresponding to each particle.

Cryogenic electron microscopy (Cryo-EM) was performed to characterize the morphology of the nanoparticles at pH 7.4 at the Ian Holmes Imaging Center (The University of Melbourne). The sample solution (3.5 μL) was placed on a glow-discharged lacey formvar/carbon coated 300 mesh copper grid (ProSciTech), then using the Vitrobot Mark IV automated vitrification (FEI company, Inc.), the grid was blotted once for 4 s and plunged into liquid ethane cooled by liquid nitrogen. The grid was loaded into a Gatan 626 cryo-specimen holder at liquid nitrogen temperature and imaged on the Talos 120C (FEI company, Inc.), operating at 120 kV accelerating voltage and low dose conditions. The Cryo-TEM images were recorded on a CETA 4 × 4k CMOS camera at a 22 000× magnification.

The morphology of the nanoparticles at low pH was characterized by transmission electron microscopy (TEM) performed at the Ian Holmes Imaging Center (The University of Melbourne). The sample solution (20 μL) was diluted in PBS (480 μL). The diluted particle solution (5 μL) was added to a glow-discharged formvar/carbon-coated 200 mesh copper grid (ProSciTech), blotted with the edge of a piece of filter paper, washed with DI water (10 μL), blotted, stained with 2 wt.% uranyl acetate solution (10 μL) and then blotted dry with the edge of a piece of filter paper. The images were captured using a Talos 120C (FEI company, Inc.) operating at 120kV.

NanoSight (NS300, Malvern Instruments Ltd.) was used to measure the size and the concentration of particles. Nanosight analysis was conducted with five measurements (each for 1 min) at 25 °C. All measurements were performed with a dilution factor at which the number of particles per frame would be between 20 and 100. The particles were diluted at the volume ratio of 1:10 000 (particles:PBS) at pH 8.0. They were diluted at the ratio of 1:1000 for DPA_1DEA_2 and at the ratio of 1:10 000 for the other two particles (DPA_2DEA_1 and DPA_3DEA_0) at the swelling pH (based on DLS results). The measurements for DPA_1DEA_2, DPA_2DEA_1, and DPA_3DEA_0 particles were done with 33, 49, and 50 particles per frame at pH 8.0 and with 59, 32, and 35 particles per frame at the corresponding swelling pH respectively. The camera level was set to 10 and the detection threshold to 3 for all measurements.

2.3. Materials Synthesis and Methodologies

2.3.1. Synthesis of Poly(Ethylene Glycol) Macro-RAFT Agent (PEG Macro-RAFT Agent)

Steglich esterification was used to couple PEG with RAFT agent.[20–22] The reaction was modified by the alternative use of DIC instead of DCC due to its higher solubility in more solvents including DCM resulting in more effective purification through chromatographic column.[22] mPEG-OH (3.00 g, 1.50 mmol), RAFT agent 4-cyano-4-(thiobenzoylthio)pentanoic acid (0.84 g, 3.00 mmol), and DMAP (0.03 g, 0.21 mmol) in 20 mL dry DCM were mixed in a round bottom flask. The mixture was cooled down to 0 °C using an ice bath, then DIC (0.47 mL, 3.00 mmol) was injected dropwise onto the stirred solution under inert atmosphere slowly. After reaction overnight at room temperature, the reaction mixture was then filtered, and the white solid by-product was washed with DCM. The combined solution was loaded on a silica column (≈ 3 × 10 cm size) and ethyl acetate (100 mL), DCM (100 mL), and methanol/DCM (10:90%, v/v) were successively eluted, while the pink fraction after methanol/DCM was collected. The solution was concentrated and then solidified after the addition-evaporation of diethyl ether. The solid product was dried under vacuum. The number average molecular weight (M_n) of the product was expected to be 2279.38 Da (≈ 2000 for mPEG and 279.38 for RAFT agent). ^{1}H NMR (400 MHz, $CDCl_3$) δ = 7.86–7.92 (m, 2H, *ortho*-C_6H_5), 7.59–7.52 (m, *para*-C_6H_5), 7.42–7.34 (m, 2H, *meta*-C_6H_5), 4.34–4.15 (m, 2H, –$CO_2CH_2CH_2$–), 3.85–3.50 (m, $CH_3O(C_2H_4O)_{43}$–), 3.36 (s, 2H, CH_3O–), 2.85–2.66 (m, 2H, –$CH_2CH_2C(CN)$–), 2.67–2.51 (m, 1H, –$CH_2CH_2C(CN)$–), 2.48–2.37 (m, 1H, –$CH_2CH_2C(CN)$–), 1.92 (s, 2H, –$C(CN)CH_3$). ^{1}H NMR spectrum with full assignment is shown in Figure S1 (Supporting Information) The GPC showed a$M_{n,GPC}$ 4100 Da, $Đ$ 1.11 (PMMA standard), GPC trace given in Figure S2, (Supporting Information).

2.3.2. Synthesis of PEG-b-PBA

PEG-*b*-PBA was prepared by reversible addition–fragmentation chain transfer (RAFT) polymerization. BA (5.62 g, 43.87 mmol), PEG macro-RAFT agent (2 g, 0.88 mmol), and AIBN (0.01 g, 0.09 mmol) were dissolved in 1,4-dioxane (10.92 mL, 4 M for BA) and placed in a Schlenk flask equipped with a magnetic bar to achieve the molar ratio 50:1:0.1. The Schlenk flask with the reaction mixture was degassed over five freeze–thaw–pump cycles. After the last cycle, the Schlenk flask was backfilled with nitrogen gas. The Schlenk flask containing the degassed reaction mixture was placed in an oil bath preheated to 60 °C and stirred at 60 °C to achieve the polymerization conversion of ≈ 25% and give DP_{BA} ≈ 10 monitored by ^{1}H NMR. The reaction was terminated by the exposure of the reaction mixture to air and the polymer was purified via precipitation in cold hexane three times to give the final pink solid product. ^{1}H NMR spectrum with full assignment, MALDI-TOF result and GPC trace are presented in Figures S3 and S2 (Supporting Information) ($DP_{BA,\ NMR}$ = 10, $M_{n,NMR}$ 3534 Da, $M_{n,\ MALDI}$ 3592.779 Da, $M_{n,GPC}$ 5800 Da, $Đ$ = 1.11 (PMMA standard)).

Table 1. The ingredients added to the reaction mixture to form particles.

Particles	DPA [mg]	DEA [mg]	PEGMA [mg]	Cy5-MA [mg]	DMF [µL]
DPA_1DEA_2	100	200	150	0.1	5
DPA_2DEA_1	200	100	150	0.5	25
DPA_3DEA_0	300	0	150	0.5	25

2.3.3. Synthesis of Methacrylic Acid N-Hydroxysuccinimide

To a suspension of methacrylic acid (8.43 mL, 100 mmol), *N*-hydroxysuccinimide (11.5 g, 100 mmol), and DMAP (244 mg, 2 mmol) in CH_2Cl_2 (150 mL) was added a solution of DCC (23 g, 110 mmol) at 0 °C. After stirring at room temperature for 18 h, the reaction was cooled to 4 °C and kept for 2 h at this temperature. Then after warming to room temperature, the mixture was filtered, and the filtrate was concentrated under reduced pressure. The solid residue was then recrystallized in diethyl ether to obtain pale yellow crystals (14.2 g, 71%). ^{1}H NMR (400 MHz, $CDCl_3$) δ 6.49–6.31 (m, 1H), 5.89–5.60 (m, 1H), 2.85 (s, 4H), 2.04 (s, 3H). ^{13}C NMR (101 MHz, $CDCl_3$) δ 169.22, 162.13, 131.84, 130.48, 25.60, 18.23 (Figure S4, Supporting Information).

2.3.4. Synthesis of Cyanine 5 Amine Methacrylamide Monomer

Cy5 amine (25 mg, 0.038 mmol) and methacrylic acid *N*-hydroxysuccinimide (71 mg, 0.39 mmol) were dissolved in dry DMF (2 mL), under nitrogen atmosphere followed by addition of TEA (11.61 mg, 0.11 mmol). After stirring overnight at room temperature, the reaction mixture was purified by column chromatography over silica (10% MeOH in DCM as the eluent). A dark blue solid was obtained (≈ 25 mg, quantitative). HRMS (ESI) m/z $[M]^+$ called for $C_{42}H_{57}N_4O_2^+$ 649.4477, found 649.4366. ^{1}H NMR spectrum and the mass spectroscopy result are shown in Figure S5 (Supporting Information), which are in agreement with literature.[23]

2.3.5. Synthesis of Emulsion Particles

Emulsion particles were synthesized by emulsion polymerization in PBS at pH 8.0. PEG-*b*-BA (25.00 mg, 0.007 mmol) and ABCVA (7.50 mg, 0.027 mmol) were dissolved in PBS (pH 8.0, 20 mL). After readjusting mixture to pH 8.0, the size of pre-micelles was reduced from ≈ 350 nm to ≈ 55 nm via sonication (by digital ultrasonic cleaner for 5 min). The mixture (containing the stabilizers, initiator, and PBS) was degassed for 30 min via nitrogen bubbling at room temperature. The particle composition was limited to a maximum of 66% molar ratio DEA (as in DPA_2DEA_1) as stable emulsion particles were not made with only DEA. To make dye-labeled nanoparticles, the mixture of additives (**Table 1**) and 5 mL of PBS at pH 8.0 were injected into the reaction flask simultaneously over ≈ 15 min while stirring at 1000 rpm. One milliliter of PBS at pH 8.0 was used to rinse the syringe. After 1 h, the reaction was terminated by exposure to air. The excess monomer and DMF was removed by dialysis against PBS at pH 8.0 using a 100 kDa dialysis tube over a few days (3–4 days). The schematic structure of particles is shown in **Scheme 2**.

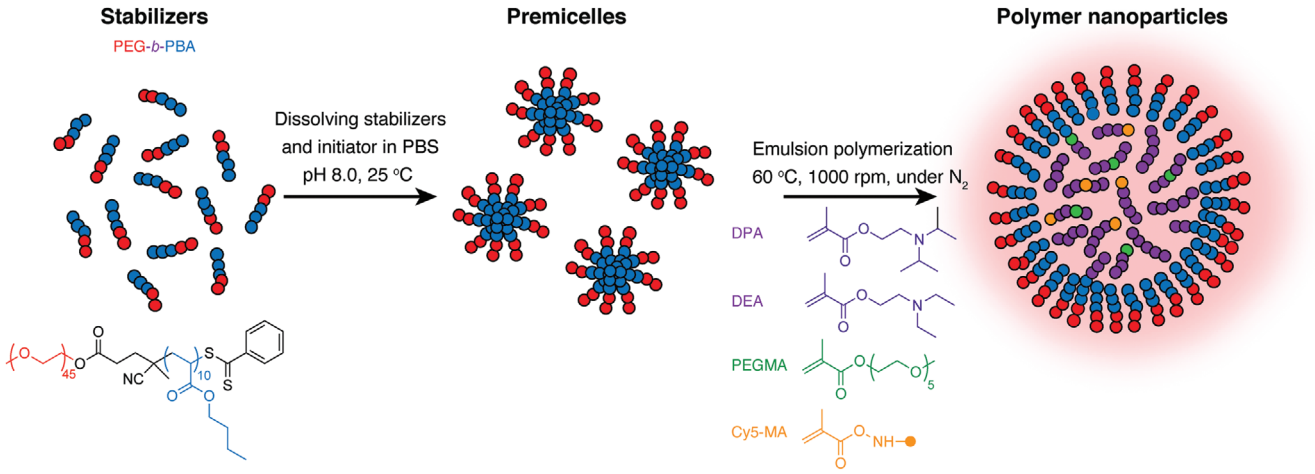

Scheme 2. Schematic demonstrating the synthesis of dye-labelled particles with PEG-*b*-PBA shell and pH-responsive core.

2.3.6. The Kinetic of Emulsion Polymerization by DLS

The properties of all particles were monitored using DLS over 4 h. These results showed an increase in the particle size, and a decrease in the swelling ratio after 1 h reaction time (data not shown). This suggested that unwanted cross-linking was happening during polymerization. Therefore, 1 h polymerization time was selected to allow the synthesis of smaller particles with higher swelling capability.

2.3.7. The Kinetic of Emulsion Polymerization by GPC

GPC traces of particles DPA_3DEA_0 at 30 and 60 min are shown in Figure S2 (Supporting Information). The shoulder (with the peak at ≈ 17–17.5 min) in the GPC traces for the particles is related to the core polymer that is larger than short stabilizers (with the peak at ≈ 21 min). The slight movement of the shoulder is seen for the particle at 60 min toward the left side compared to the particle at 30 min suggesting that the core polymer is getting larger over time. This suggests some incorporation of the stabilizer into the nanoparticle structure.

2.3.8. The Kinetic and Monomer Conversion of Emulsion Polymerization by ^{1}H NMR

The kinetics of the reaction was studied for the DPA_3DEA_0 particle over 2 h. PEG-*b*-PBA stabilizers (12.5 mg, 0.0035 mmol) and ABCVA (3.75 mg, 0.013 mmol) were mixed in 12.5 mL of PBS in D_2O at pH 8.0. Then pH was readjusted to pH 8.0. After ≈ 5 min sonication, the solution of initial micelles ≈ 50 nm was degassed using nitrogen bubbling for 30 min at room temperature. DPA (150 mg, 0.70 mmol) and PEGMA (75 mg, 0.25 mmol) were injected into the solution at 60 °C for ≈ 15 min while stirring vigorously (1000 rpm). The syringe was rinsed with extra 0.5 mL of PBS in D_2O at pH 8.0. The reactions were terminated after 0.5, 1, 1.5, and 2 h. Then, maleic acid (2 mg, 0.017 mmol) was added to 1 mL of the particle's solution. The conversions were calculated by comparing the ^{1}H NMR integrations for the vinyl protons of DPA and PEGMA before and after reaction. ^{1}H NMR spectra of particles at 0 min and 60 min in Figure S6 (Supporting Information) shows that ≈ 40% of monomers were converted to polymer after 1 h (data not shown for other reaction times).

2.3.9. Buffering Capacity

The synthesized particles were dialyzed against water to remove salts. After freeze-drying, the dry powder of particles (≈ 2 mg) was dissolved in 5.0 mL of NaCl (0.15 M, pH 3.0) and the pH was then readjusted to pH 3.0. The particle solutions were titrated against 0.02 M NaOH, and their pH was measured. The buffering capacity of the particles was defined as the percentage of ionized amine groups from pH ≈ 6 to ≈ 7 (buffering region) and calculated on the basis of Equation (1):[24]

$$\text{Buffering capacity } (\%) = 100(\Delta V_{\text{NaOH}} \times 0.02\text{M})/N_{\text{mol}} \quad (1)$$

where ΔV_{NaOH} is the volume of 0.02 M NaOH, which changes the pH of the particles in the buffering region by one unit, and N_{mol} is the total moles of amine groups in the particle.

2.4. Biological Assays

The association of mouse embryonic fibroblast NIH-3T3 cells at the particle concentrations used was confirmed through the flow cytometry assay and it was believed that this suggests sufficient cells will have internalized to make it a suitable cell model for studying endosomal escape.[25,26] Therefore, NIH-3T3 cells were used for biological assays.

In the Alamar Blue viability assay, NIH-3T3 cells were seeded at 10 000 cells per well in a clear-bottom 96-well black plate and incubated overnight at 37 °C with 5% CO_2. Standard nanoparticle solutions were added to the cells (in triplicates) to a final concentration of 0.19, 0.39, 0.78, 1.56, 3.125, 6.25, 12.5, 25, and 50×10^9 particles mL^{-1}. Cells were incubated with particles for 4 h at 37 °C with 5% CO_2. The media was replaced with fresh prewarmed media for overnight culture. Alamar Blue reagent

(Thermo Fisher) was incubated with cells as in the manufacture's protocol for 4 h at 37 °C with 5% CO_2. The fluorescence at 590 nm was read using a fluorescence plate reader (Clariostar, BMG).

To study the association of particles with cells by flow cytometry, NIH-3T3 cells were maintained in DMEM supplemented with high glucose (GlutaMAX) and 20% fetal bovine serum. Cells were cultured at 37 °C in a humidified incubator with 5% atmospheric CO_2. For flow cytometry, cells were seeded at 100 000 cells per well in 24-well plates with 400 µL of media. Cy5 nanoparticles were added to cells to a final concentration of 5, 10, 20, and 50 × 10^9 particles mL^{-1} in culturing medium and incubated for 4 h at 37 °C with 5% CO_2. After incubation, the media was removed, and cells were washed three times on a plate with 400 µL of PBS. The cells were detached and transferred to a 96-well V-bottom plate (Corning, Sigma–Aldrich) and spun at 400 × *g* for 5 min. The supernatant was discarded, and cells were resuspended in 150 µL of 1% BSA−PBS. Samples were run on an S1000EXi flow cytometer (Stratedigm, Inc.). Particle concentrations of 5, 10, 20, and 50 × 10^9 particles mL^{-1} were analyzed for each sample, and the data were analyzed using FlowJo 8.7 software (FlowJo, LLC). The association was normalized to the amount of loaded cyanine 5 according to the absorbance of the particles at 646 nm. For flow cytometry gating strategy, cells were gated on side and forward side scattering gates for cells population. Single cells population were focusing on forward side scattering area versus side scattering heights. Live cells population were based on fluorescence of the viability dye. The geometric means were extracted for further analysis.

For the calcein assay, NIH-3T3 cells were seeded at 10 000 cells per well (100 µL volume) in an optically clear-bottom 96-well plate overnight. Standard nanoparticle solutions were added to cells to a final concentration of 10 × 10^9, 20 × 10^9, and 50 × 10^9 particles mL^{-1} in culturing medium and incubated for 2 h at 37 °C with 5% CO_2. The calcein solution was then added to a final concentration of 100 µg mL^{-1} for another 2 h of incubation. The cells were carefully washed five times with FluoroBrite with 10% FBS to remove excess calcein. Live cell imaging was performed using an Olympus IX83 microscope with a 20 × 0.9 NA air objective with a standard "Pinkel" DAPI/FITC filter set from Semrock. Images were analyzed with ImageJ.

3. Results and Discussion

3.1. Particle Assembly and Swelling Behavior

A series of pH-swellable nanoparticles were synthesized with a pH-responsive core and a stealth pH-insensitive shell. The shell of the nanoparticle was formed by a PEG-*b*-PBA macro-RAFT agent, a mixture of monomers DPA/DEA/PEGMA/Cy5-MA (Table 1) was then polymerized as a pH-responsive core using emulsion polymerization. Three dye-labeled particles with various ratios of DPA and DEA (1:2, 2:1, and 3:0 (w/w)) were synthesized (Table 1) that will be subsequently referred to as DPA_1DEA_2, DPA_2DEA_1, and DPA_3DEA_0. To study the pH-dependent behavior of particles, the hydrodynamic diameter and the polydispersity (PI) of particles equilibrated in PBS (≈ 2 min) at 37 °C with pH ranging from 5.0 to 7.4 was measured by DLS. As shown in **Figure 1**A, the three particles, DPA_1DEA_2, DPA_2DEA_1, and DPA_3DEA_0, have a diameter of ≈ 100 nm at pH 7.4, and swell to

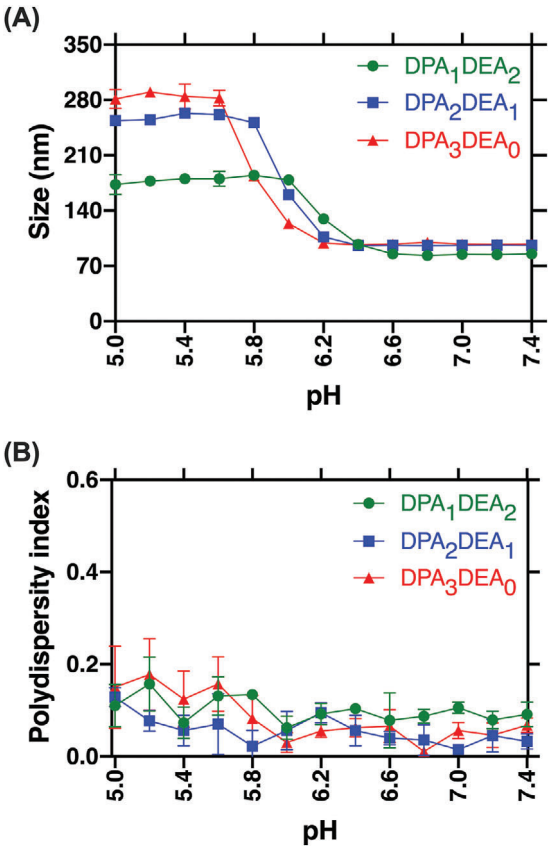

Figure 1. A) pH-induced swelling of DPA_1DEA_2, DPA_2DEA_1 and DPA_3DEA_0 particles at 37 °C. Mean particle size as a function of pH was measured by DLS. B) Polydispersity index of DPA_1DEA_2, DPA_2DEA_1 and DPA_3DEA_0 particles as a function of pH was measured by DLS.

185, 260, and 290 nm at low pH, respectively. The pH at which swelling occurred was tuned by changing the particle composition, with DPA_1DEA_2 particles swelling at pH 6.0, DPA_2DEA_1 particles swelling at pH 5.8, and DPA_3DEA_0 particles swelling at pH 5.6. This trend was expected, as a higher amount of DPA (which has a lower pK_a) leads to an onset of swelling at a lower pH. As shown in Figure 1B, all particles were monodisperse with PI lower than 0.2 at physiological pH. This low PI was maintained even after swelling. The particles showed a swelling ratio of ≈ 120%, 175%, and 200% as DPA increased (Figure 1A). We postulate that the different swelling ratios might be due to changes in the hydrophobicity of the DPA and DEA monomers leading to differences in core particle structure. The characterization of particle stability was performed using DLS measurement over 5 days at both pH 7.4 and the pH at which the maximum swelling occurred at 37 °C. They stayed stable at pH 7.4 with a low PI as shown in Figure S7 (Supporting Information). However, the DPA_1DEA_2 started aggregating at low pH (6.0) after the second day indicated by the PI increasing to higher than 0.2. The size and monodispersity of particles at pH 7.4 were also confirmed by cryo-EM as shown in **Figure 2**. Cryo-EM was also performed for the particles at low pH, however, the contrast was extremely low (images are not shown). We believe this was due to the hydrogel nature of these systems at low pH. TEM (negative staining) was

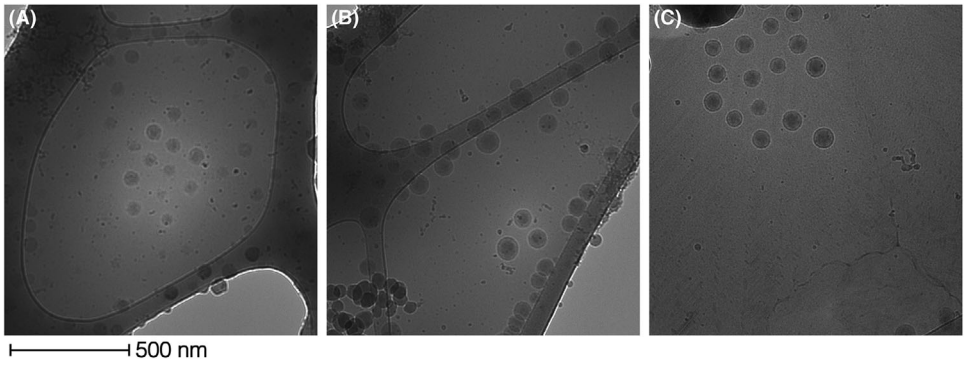

Figure 2. Cryo-EM images of particles. A) DPA_1DEA_2, B) DPA_2DEA_1, and C) DPA_3DEA_0 at pH 7.4. The larger structure in the images corresponds to the grid.

then done at low pH values and reported in Figure S8 (Supporting Information) confirming the swelling behavior of particles.

The swelling behavior of particles was also confirmed by NanoSight. NanoSight tracks the movement of individual particles, yielding both particle size distribution and concentration. As shown in **Figure 3**, the DPA_1DEA_2, DPA_2DEA_1, and DPA_3DEA_0 particles swell from 90–100 nm at pH 7.4 to 140 nm at pH 6.0, 215 nm at pH 5.8 and 220 nm at pH 5.6, respectively, which is in good agreement with the DLS data (Table S1, Supporting Information). The concentration of the DPA_1DEA_2 particles decreased by ≈ 75% upon reduction in pH, while the DPA_2DEA_1 and DPA_3DEA_0 particles' concentration decreased by only 25–30%. This decrease in particle concentration at lower pH suggests that some of the particles fell apart due to the protonation of the particle structure at low pH.

3.2. Cytotoxicity of Particles via Alamar Blue Assay

An important feature of delivery systems is to effectively deliver therapeutics without causing toxicity and damaging nontargeted cells. Hence, before analyzing the endosomal escape properties of the particles, their toxicity was scrutinized. The viability of NIH-3T3 cells after incubation with particles at various concentrations was determined using the Alamar Blue assay. **Figure 4** shows the cell viability for all three nanoparticles. The particles showed no decrease in viability even at high particle concentrations of 50×10^9 particles mL^{-1}.

Cell viability is reported relative to untreated cells and measured using the Alamar Blue assay after incubating the cells with particles for 4 h then incubating for a further 4 h in cell media. Error bars are standard deviation of the experiment conducted in triplicate.

3.3. Particle-Cell Association via Flow Cytometry

The association of particles with cells was evaluated by flow cytometry.[27–29] **Figure 5** shows the different cellular association after the incubation with cells at 37 °C for 2 h (Flow cytometry gating strategy is shown in Figure S9, Supporting Information). Particle concentrations of 5, 10, 20, and 50×10^9 particles mL^{-1} were analyzed for each sample and the association was normalized to the amount of Cy5 based on the absorbance of the particles at 646 nm. The normalized fluorescence signal allows a direct comparison of association across all particles, as shown in Figure 5. Cells with the higher level of DPA showed an increase in the mean fluorescence intensity (MFI) indicating the higher association of particles to NIH-3T3 cells. This suggests variation in the particle composition changes the interactions with cells, which could be due to particle morphology as we have seen in earlier work.[10] This is possibly due to the higher hydrophobicity of the DPA monomer in this case. As expected, at higher concentrations of particles, association with cells was higher. Zeta potential showed there were no significant differences in charge between the particles at physiological pH (Table S2, Supporting Information).

3.4. Buffering Capacities of Particles

The buffering capacity of particles was measured as shown in **Figure 6** to better understand the behavior of particles in endosomes. All three particles, DPA_1DEA_2, DPA_2DEA_1, and DPA_3DEA_0, were able to buffer in the physiological pH range with pK_a values of ≈ 6.8, ≈ 6.7, ≈ 6.6, and with buffering capacities of 87%, 99%, and 132% respectively (Table S3, Supporting Information). It is interesting to note the higher buffering capacity of the DPA_3DEA_0 system suggests it's higher potential to facilitate endosomal escape. All these nanoparticles demonstrate pH-induced swelling and buffering capacity and thus they are effective models to investigate both the proton-sponge effect and pH-induced swelling within an endosome/lysosome.

3.5. Endosomal Escape Capability of Particles via Calcein Assay

To assess the endosomal escape capability of particles following particle uptake by cells, a calcein assay was used.[30] Calcein is a membrane-impermeable green fluorophore that has generated significant interest as a model small molecule and a tracer.[11] Calcein was added to cells without particles as the control and with particles to test their behaviour in endo/lysosomal compartments. After a 2 h incubation of cells with particles and a further 2 h incubation of cells and particles with calcein at 37 °C, excess extracellular calcein and particles were washed thoroughly from

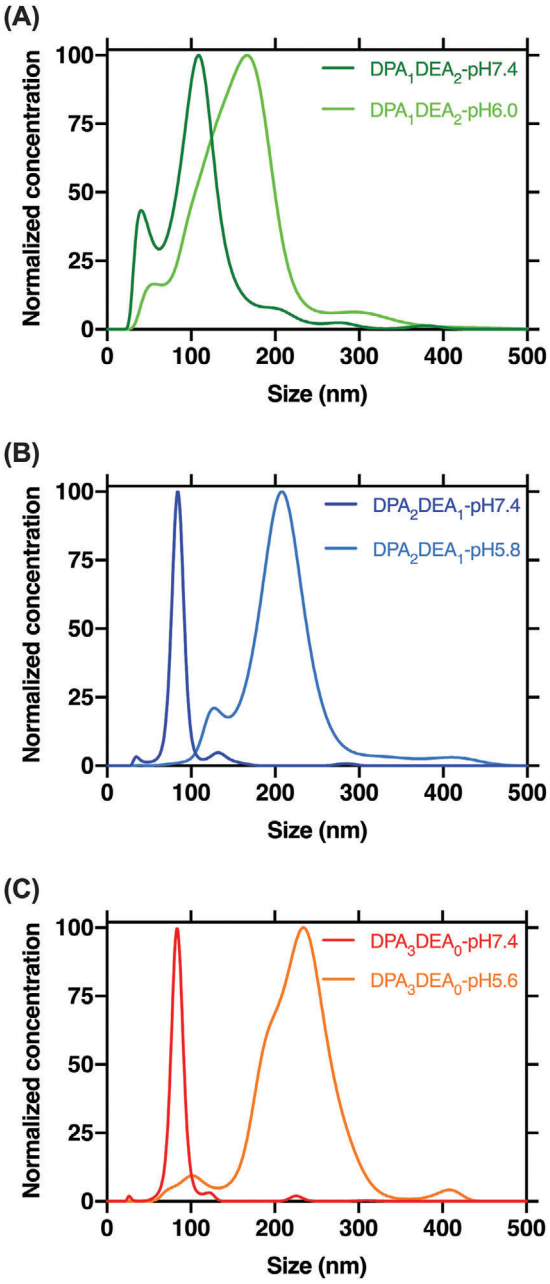

Figure 3. Analysis of particle concentration and size. A) DPA_1DEA_2, B) DPA_2DEA_1, and C) DPA_3DEA_0 at pH 7.4 (25 °C) and at the maximum swelling pH (the maximum swelling pH was estimated using DLS at 37 °C) via NanoSight. The size traces were normalized to the modal particle size.

the cells. The cells with different particle concentrations were then imaged. **Figure 7** shows the fluorescence microscopy images of particles at 50×10^9 particles mL^{-1} (the images at lower concentrations can be found in Figure S10, Supporting Information). If the particles destabilize the endosomal membrane, calcein will be released into the cell, yielding an intense green, fluorescent pattern dispersed through the entire cell. If, however, there is no endosomal escape, calcein will remain trapped in endosomes, yielding a dim, punctate distribution.[30,632] As shown

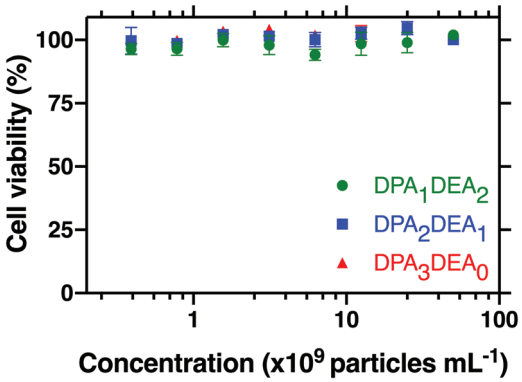

Figure 4. Cell viability of DPA_1DEA_2, DPA_2DEA_1, and DPA_3DEA_0 particles in NIH-3T3 cells.

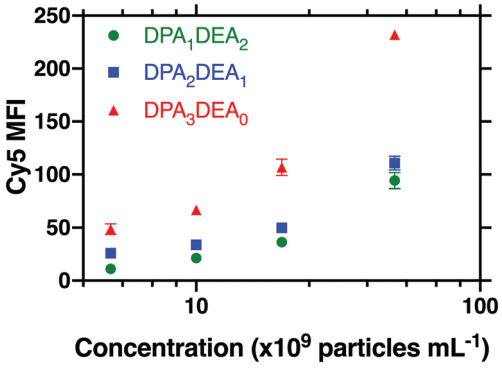

Figure 5. Flow cytometry histogram showing the MFI of particles DPA_1DEA_2, DPA_2DEA_1, and DPA_3DEA_0 in NIH-3T3 cells.

in Figure 7, cells with and without particles showed a punctuate distribution of fluorescence suggesting negligible endosomal escape. Interestingly, there was no difference in the distribution of calcein even though the DPA_3DEA_0 system had better swelling percentage and buffering capacity, suggesting these properties did not enhance the endosomal escape potential of the system. Previous work by Irvine et al. reported that a successful endosomal escape was observed for the particles with ≈ 280% swelling.[11] This suggests that pH-induced swelling of

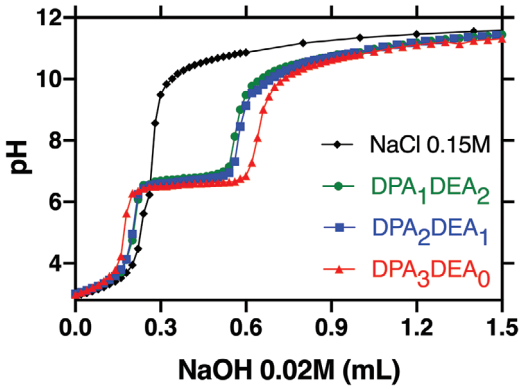

Figure 6. The particles buffering curve, prepared using NaCl 0.15 M, particles DPA_1DEA_2, DPA_2DEA_1, and DPA_3DEA_0.

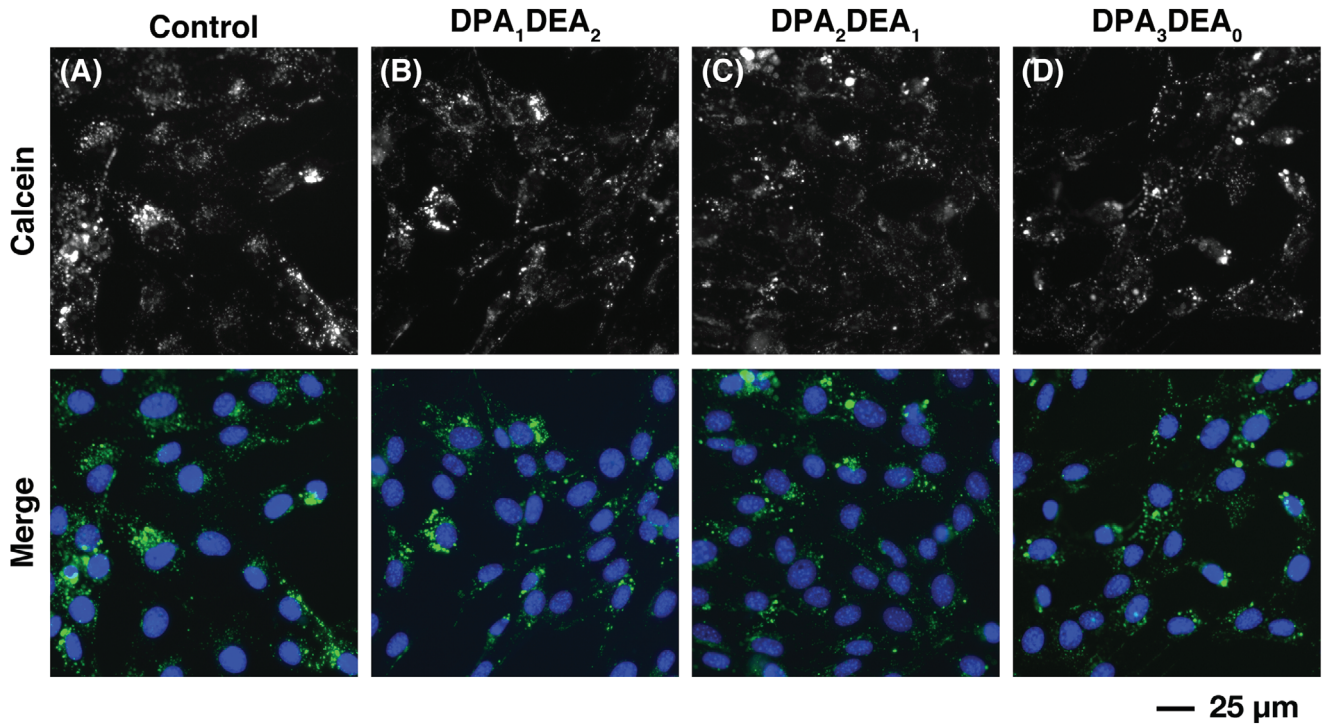

Figure 7. Fluorescence microscopy images of dye-labelled particles with calcein, A) the control (cells incubated with just calcein), B) DPA_1DEA_2 particles, C) DPA_2DEA_1 particles, and D) DPA_3DEA_0 particles at the concentration of 50×10^9 particles mL^{-1} showing a distinct punctate fluorescence of calcein throughout the cells. The nuclei were stained with Hoechst 33 342 (blue).

120–200% is not sufficient on its own to drive endosomal escape and that more needs to be understood about this potential mechanism.

In addition to particle swelling, the particles exhibit a buffering capacity that should induce a proton-sponge effect, this is also different throughout the series of nanoparticles, however no difference in endosomal escape was observed. In recent years there are a growing number of reports suggesting limitations with the proton-sponge mechanism.[10,15,33] As we observed no endosomal escape with any of these formulations, this provides further evidence to question the role of the proton-sponge effect in inducing endosomal escape.

4. Conclusion

A series of pH-responsive swellable particles with different ratios of two pH-responsive monomers (DPA and DEA), DPA_1DEA_2, DPA_2DEA_1, and DPA_3DEA_0, were synthesized and exhibited pH-dependent swelling when the pH decreased to pH 6.0, 5.8, and 5.6 respectively. When the pH was decreased from 7.4 to below their transition points, the particles swelled to between 120% and 200% of their original size, depending on the polymer composition. These particles were used to understand pH-induced swelling and the proton-sponge effect as potential endosomal escape mechanisms for nanoparticle delivery systems. The particles showed strong buffering capacity as well as the ability to associate with cells, however there was no evidence of endosomal escape using the calcein assay. These results open up questions about the limitations of pH-induced swelling and proton-sponge effect as a general endosomal escape method. It is clear that more needs to be understood about these mechanisms in order to improve the endosomal escape and thus the effective delivery of nanoparticles.

Supporting Information

Supporting Information is available from the Wiley Online Library or from the author.

Acknowledgements

This work was supported by the Australian Research Council Discovery Project (DP180100844). The authors would like to thank Professor Eric Hanssen, Dr Andrew Leis, Dr Hamish Brown and Dr Sepideh Valimehr for the valuable discussion and guidance for the Cryo-EM and TEM imaging.

Open access publishing facilitated by The University of Melbourne, as part of the Wiley - The University of Melbourne agreement via the Council of Australian University Librarians.

Conflict of Interest

The authors declare no conflict of interest.

Data Availability Statement

The data that support the findings of this study are available from the corresponding author upon reasonable request.

Keywords

buffering, emulsion, particles, pH-responsive, endosmal escape

Received: November 2, 2021
Revised: February 2, 2022
Published online: March 4, 2022

[1] Y. Yuan, B. Liu, *Chem. Sci.* **2017**, *8*, 2537.
[2] N. Deirram, S. S. Kermaniyan, A. P. R. Johnston, G. K. Such, *Aust. J. Chem.* **2021**, *74*, 514.
[3] Y. Gao, J. Xu, C. Zhang, H. Venugopal, S. S. Kermaniyan, G. Such, C. Ritchie, *ACS Appl. Nano Mater.* **2020**, *3*, 11247.
[4] U. Nayanathara, S. S. Kermaniyan, G. K. Such, *Macromol. Rapid Commun.* **2020**, *41*, e2000298.
[5] N. Deirram, C. Zhang, S. S. Kermaniyan, A. P. R. Johnston, G. K. Such, *Macromol. Rapid Commun.* **2019**, *40*.
[6] S. A. Smith, L. I. Selby, A. P. R. Johnston, G. K. Such, *Bioconjugate Chem.* **2019**, *30*, 263.
[7] J. Chen, J. Li, J. Zhou, Z. Lin, F. Cavalieri, E. Czuba-Wojnilowicz, Y. Hu, A. Glab, Y. Ju, J. J. Richardson, F. Caruso, *ACS Nano* **2019**, *13*, 11653.
[8] J. J. Rennick, A. P. R. Johnston, R. G. Parton, *Nat. Nanotechnol.* **2021**, *16*, 266.
[9] W. Wu, L. Luo, Y. Wang, Q. Wu, H. B. Dai, J. S. Li, C. Durkan, N. Wang, G. X. Wang, *Theranostics* **2018**, *8*, 3038.
[10] N. Kongkatigumjorn, C. Cortez-Jugo, E. Czuba, A. S. Wong, R. Y. Hodgetts, A. P. Johnston, G. K. Such, *Macromol. Biosci.* **2017**, *17*.
[11] Y. Hu, T. Litwin, A. R. Nagaraja, B. Kwong, J. Katz, N. Watson, D. J. Irvine, *Nano Lett.* **2007**, *7*, 3056.
[12] R. A. Jones, C. Y. Cheung, F. E. Black, J. K. Zia, P. S. Stayton, A. S. Hoffman, M. R. Wilson, *Biochem. J.* **2003**, *372*, 65.
[13] K. I. Cupic, J. J. Rennick, A. P. Johnston, G. K. Such, *Nanomedicine* **2019**, *14*, 215.
[14] J. O. You, D. T. Auguste, *Nano Lett.* **2009**, *9*, 4467.
[15] A. M. Funhoff, C. F. van Nostrum, G. A. Koning, N. M. Schuurmans-Nieuwenbroek, D. J. Crommelin, W. E. Hennink, *Biomacromolecules* **2004**, *5*, 32.
[16] S. Roy, D. Zhu, W. J. Parak, N. Feliu, *ACS Nano* **2020**, *14*, 8012.
[17] I. Richard, M. Thibault, G. De Crescenzo, M. D. Buschmann, M. Lavertu, *Biomacromolecules* **2013**, *14*, 1732.
[18] T. Bus, A. Traeger, U. S. Schubert, *J. Mater. Chem. B* **2018**, *6*, 6904.
[19] A. Tamura, M. Oishi, Y. Nagasaki, *Biomacromolecules* **2009**, *10*, 1818.
[20] H. T. Ho, M. E. Levere, S. Pascual, V. Montembault, N. Casse, A. Caruso, L. Fontaine, *Polym. Chem.* **2013**, *4*, 675.
[21] H. T. Ho, M. L. Bohec, J. Frémaux, S. Piogé, N. Casse, L. Fontaine, S. Pascual, *Macromol. Rapid Commun.* **2017**, *38*.
[22] M. Tsakos, E. S. Schaffert, L. L. Clement, N. L. Villadsen, T. B. Poulsen, *Nat. Prod. Rep.* **2015**, *32*, 605.
[23] A. K. Pearce, B. E. Rolfe, P. J. Russell, B. W. C. Tse, A. K. Whittaker, A. V. Fuchs, K. J. Thurecht, *Polym. Chem.* **2014**, *5*, 6932.
[24] A. Alazzo, T. Lovato, H. Collins, V. Taresco, S. Stolnik, M. Soliman, K. Spriggs, C. Alexander, *J. Interdiscip. Nanomed.* **2018**, *3*, 38.
[25] N. Kongkatigumjorn, S. A. Smith, M. Chen, K. Fang, S. Yang, E. R. Gillies, A. P. R. Johnston, G. K. Such, *ACS Appl. Nano Mater.* **2018**, *1*, 3164.
[26] B. C. Evans, R. B. Fletcher, K. V. Kilchrist, E. A. Dailing, A. J. Mukalel, J. M. Colazo, M. Oliver, J. Cheung-Flynn, C. M. Brophy, J. W. Tierney, J. S. Isenberg, K. D. Hankenson, K. Ghimire, C. Lander, C. A. Gersbach, C. L. Duvall, *Nat. Commun.* **2019**, *10*, 5012.
[27] R. Qi, Y. Z. Li, C. Chen, Y. N. Cao, M. M. Yu, L. Xu, B. He, X. Jie, W. W. Shen, Y. N. Wang, M. A. van Dongen, G. Q. Liu, M. M. Banaszak Holl, Q. Zhang, X. Ke, *J. Controlled Release* **2015**, *210*, 160.
[28] A. L. Barran-Berdon, D. Pozzi, G. Caracciolo, A. L. Capriotti, G. Caruso, C. Cavaliere, A. Riccioli, S. Palchetti, A. Lagana, *Langmuir* **2013**, *29*, 6485.
[29] L. I. Selby, C. M. Cortez-Jugo, G. K. Such, A. P. R. Johnston, *Wiley Interdiscip. Rev.: Nanomed. Nanobiotechnol.* **2017**, *9*.
[30] G. K. Such, Y. Yan, A. P. Johnston, S. T. Gunawan, F. Caruso, *Adv. Mater.* **2015**, *27*, 2278.
[31] A. S. Wong, S. K. Mann, E. Czuba, A. Sahut, H. Liu, T. C. Suekama, T. Bickerton, A. P. Johnston, G. K. Such, *Soft Matter* **2015**, *11*, 2993.
[32] S. L. Y. Teo, J. J. Rennick, D. Yuen, H. Al-Wassiti, A. P. R. Johnston, C. W. Pouton, *Nat. Commun.* **2021**, *12*, 3721.
[33] R. V. Benjaminsen, M. A. Mattebjerg, J. R. Henriksen, S. M. Moghimi, T. L. Andresen, *Mol. Ther.* **2013**, *21*, 149.